nature photonics

SUPPLEMENTARY INFORMATION

DOI: 10.1038/NPHOTON.2012.245

A microchip optomechanical accelerometer – Supplementary Information

Alexander G. Krause,[1] Martin Winger,[1] Tim D. Blasius,[1] Qiang Lin,[2] and Oskar Painter[1]

[1]*Thomas J. Watson, Sr., Laboratory of Applied Physics, California Institute of Technology, Pasadena, CA 91125, USA*

[2]*School of Engineering and Applied Sciences, University of Rochester, Rochester, New York 14627, USA*

(Dated: June 20, 2012)

I. OSCILLATOR SUSCEPTIBILITY

The oscillator susceptibility $\chi(\omega)$ given in the main text follows from the differential equation of the harmonic oscillator:

$$m\ddot{x} + m\gamma\dot{x} + m\omega_m^2 x = F_{\rm appl}. \tag{S1}$$

Transforming to Fourier space, this reads

$$-\omega^2 x + i\omega\gamma x + \omega_m^2 x = \frac{F_{\rm appl}(\omega)}{m}. \tag{S2}$$

With $F_{\rm appl}(\omega)/m = a_{\rm appl}$, this yields the accelerometer response

$$\begin{aligned} x(\omega) &= \chi(\omega) a_{\rm appl}(\omega) \\ &= \frac{1}{\omega_m^2 - \omega^2 + i\frac{\omega\omega_m}{Q_m}} a_{\rm appl}(\omega). \end{aligned} \tag{S3}$$

This function has the following properties:

$$\chi(0) = \frac{1}{\omega_m^2} = \frac{m}{k}, \tag{S4}$$

$$\chi(\omega_m) = -i\frac{Q_m}{\omega_m^2} = -iQ_m\chi(0), \tag{S5}$$

$$\chi(\omega \gg \omega_m) \propto \frac{1}{\omega^2}. \tag{S6}$$

For the device studied here with $\omega_m = 2\pi \times 27.5$ kHz, this gives an acceleration sensitivity of $\chi(0) = 329$ pm/g with $g = 9.81$ m/s^2.

II. TRANSMISSION FUNCTION OF SIDE-COUPLED OPEN CAVITY

In order to calculate the intensity transmission profile $T(\omega)$ of a photonic-crystal resonator side-coupled by a fiber-taper waveguide, we start from the equation of motion of $\hat{a}$, the annihilation operator of the cavity field:

$$\frac{{\rm d}\hat{a}}{{\rm d}t} = -\left(i\Delta + \frac{\kappa}{2}\right)\hat{a} + \sqrt{\frac{\kappa_e}{2}}\hat{a}_{\rm in} + \sqrt{\kappa_i}\hat{a}_{\rm i} + \sqrt{\frac{\kappa_e}{2}}\hat{a}_{-}. \tag{S7}$$

Here, $\Delta = \omega_{\rm l} - \omega_{\rm c}$ is the laser-cavity detuning, κ_e is the total taper-cavity coupling rate, $\kappa = \kappa_i + \kappa_e$ is the total cavity decay rate, with κ_i the intrinsic cavity damping rate, and $\hat{a}_{\rm in}$ is the taper input field, which together with the output field $\hat{a}_{\rm out}$ obeys the boundary condition

$$\hat{a}_{\rm in} + \hat{a}_{\rm out} = \sqrt{\frac{\kappa_e}{2}}\hat{a}. \tag{S8}$$

The last two terms on the right-hand-side of eq. (S7) represent the vacuum inputs due to coupling with the intrinsic (loss) bath of the cavity and the backward fiber taper waveguide mode, respectively (these input terms are ignored going forward as they are in the vacuum state and do not modify the classical field equations). In steady state, where $\frac{{\rm d}\hat{a}}{{\rm d}t} \equiv 0$, the intracavity field operator is

$$\hat{a}_0 = \sqrt{\frac{\kappa_e}{2}}\frac{\hat{a}_{\rm in}}{i\Delta + \frac{\kappa}{2}}. \tag{S9}$$

DOI: 10.1038/NPHOTON.2012.245

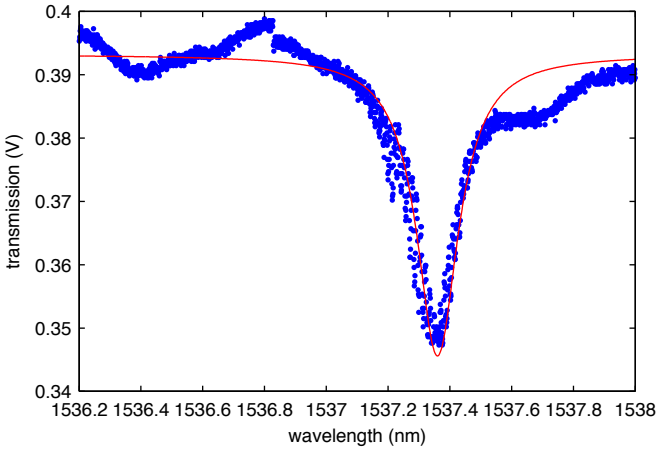

FIG. S1: **Example transmission curve of the zipper cavity.** The curve is obtained by scanning an external cavity diode laser across the cavity resonance at $\lambda_o = 1537.36$ nm while monitoring the fiber taper transmission. The resonance exhibits an optical Q-factor of $Q_o = 9{,}500$ and a transmission dip on resonance of $T_d = 0.88$.

$\hat{a}_{\rm in}$ is normalized to the power incident on the cavity $P_{\rm in}$ as $P_{\rm in} = \hbar\omega_l \langle \hat{a}_{\rm in}^\dagger \hat{a}_{\rm in} \rangle$ such that the intracavity photon number is

$$n_{\rm cav} = \langle \hat{a}^\dagger \hat{a} \rangle = \frac{\kappa_e}{2} \frac{1}{\Delta^2 + \frac{\kappa^2}{4}} \frac{P_{\rm in}}{\hbar\omega_l}. \tag{S10}$$

Combining eq. (S8) with eq. (S9) yields the intensity transmission function

$$T(\Delta) = \frac{|a_{\rm out}|^2}{|a_{\rm in}|^2} = 1 - \frac{\kappa_e}{4} \frac{2\kappa - \kappa_e}{\Delta^2 + \frac{\kappa^2}{4}}. \tag{S11}$$

This function describes a Lorentzian absorption curve that dips to $T_d = \frac{\kappa_i^2}{\kappa^2}$ at $\Delta = 0$. Figure S1 shows an example transmission curve of the device studied in this work obtained by scanning an external cavity diode laser across the fundamental resonance of the zipper cavity. The slope of the curve is given by

$$\frac{{\rm d}T}{{\rm d}\Delta} = \frac{\kappa_e}{2} \frac{2\kappa - \kappa_e}{\left(\Delta^2 + \frac{\kappa^2}{4}\right)^2} \Delta. \tag{S12}$$

Usually, we lock the probe laser to a red-side detuning of $\Delta = -\kappa/2$, where the transduction is maximum for fixed $n_{\rm cav}$. At that detuning, the intracavity photon number is given by

$$n_{{\rm cav},\kappa/2} = \left(1 - \sqrt{T_d}\right) \frac{Q_o}{\omega_o} \frac{P_{\rm in}}{\hbar\omega_l} \tag{S13}$$

and the slope of the transmission curve is

$$\left.\frac{{\rm d}T}{{\rm d}\Delta}\right|_{\Delta = -\frac{\kappa}{2}} = -\frac{\kappa_e (2\kappa - \kappa_e)}{\kappa^3} \tag{S14}$$

$$= -(1 - T_d) \frac{Q_o}{\omega_o}. \tag{S15}$$

III. DERIVATION OF THE OPTOMECHANICAL ACCELEROMETER TRANSDUCTION

Our device operates deep in the sideband unresolved regime, where $\omega_m \ll \kappa$ ($\omega_m = 2\pi \times 27.5$ kHz, $\kappa = \omega_c/Q_o = 2\pi \times 20.5$ GHz). In this regime, the intra-cavity field and hence the field transmitted through the cavity adiabatically follow changes in laser-cavity detuning $\Delta = \omega_l - \omega_c$ created by mechanical motion of the test-mass, $\Delta = g_{\rm OM} x$. In order to calculate the optical transmission change ΔT induced by a shift of the cavity resonance frequency Δ, we can therefore approximate

$$\Delta T = \frac{{\rm d}T}{{\rm d}\Delta} \Delta, \tag{S16}$$

such that the frequency component of the transmitted optical power arising from a displacement $x(\omega)$ is given by

$$P_{\mathrm{m}}(\omega) = \frac{\mathrm{d}T}{\mathrm{d}\Delta}\eta_{\mathrm{in}}P_{\mathrm{in}}g_{\mathrm{OM}}x(\omega), \tag{S17}$$

where P_{in} is the input power in the fiber taper waveguide at the zipper cavity and η_{in} quantifies the optical loss in the fiber taper waveguide between the cavity and the detector via $\eta_{\mathrm{in}} = P_{\mathrm{det}}/P_{\mathrm{in}}$, where P_{det} is the optical power reaching the detector. This formula relates frequency components of the transmitted optical power modulation to the mechanical motion of the test-mass. With eq. (S13) and eq. (S15), this becomes

$$P_{\mathrm{m}}(\Delta = \kappa/2) = (1 - T_d)\,\frac{Q_o}{\omega_o}g_{\mathrm{OM}}\,\eta_{\mathrm{in}}P_{\mathrm{in}}\,x. \tag{S18}$$

This optical power is measured on a Newport 2117 balanced photo-detector with switchable transimpedance gain (in these experiments we use $g_{\mathrm{ti}} = 49{,}600$ V/W), generating a voltage output of $V_{\mathrm{m}} = g_{\mathrm{ti}}P_{\mathrm{m}}$. An electronic spectrum analyzer (ESA) calculates the electrical power spectral density of this optical sideband in units of V_{m}^2/Z with $Z = 50\ \Omega$ and expresses it in dBm/Hz. The conversion follows the relation

$$\mathrm{PSD}_{\mathrm{ESA}}(\omega) = 10\cdot\log\left[\frac{(g_{\mathrm{ti}}P_{\mathrm{m}}(\omega))^2}{Z}\cdot 1{,}000\right]. \tag{S19}$$

Careful calibration of the parameters in eq. (S18) and eq. (S19) as well as the optical input power, allows one to calculate the optomechanical coupling g_{OM} from the magnitude of the (known) thermal Brownian motion noise of the mechanical oscillator. In the measurements presented in Figs. 2 and 3 of the main text, we have $T_d = 0.87$, $Q_o = 9{,}500$, $\omega_o = 2\pi \times 195$ THz, and $\eta_{\mathrm{in}} = 0.57$. At low optical input power, where negligible back-action cooling is being performed on the fundamental in-plane mechanical mode of the suspended test mass and the mode's effective temperature is the temperature of the room temperature bath ($T \sim 300K$), the optomechanical coupling constant is estimated to be $g_{\mathrm{OM}} = 2\pi \times 5.5$ GHz/nm from the area under the Lorentzian centered at 27 kHz of the optically transduced displacement noise PSD. This corresponds to an optical displacement sensitivity of $P_m/x = 3.7$ nW/pm for the fundamental in-plane mechanical mode of the suspended test mass. From electromagnetic finite-elements simulations we calculate $g_{\mathrm{OM}} = 2\pi \times 13.5$ GHz/nm for dimensions of the zipper cavity as measured with a scanning electron microscope, in good agreement with the measured value.

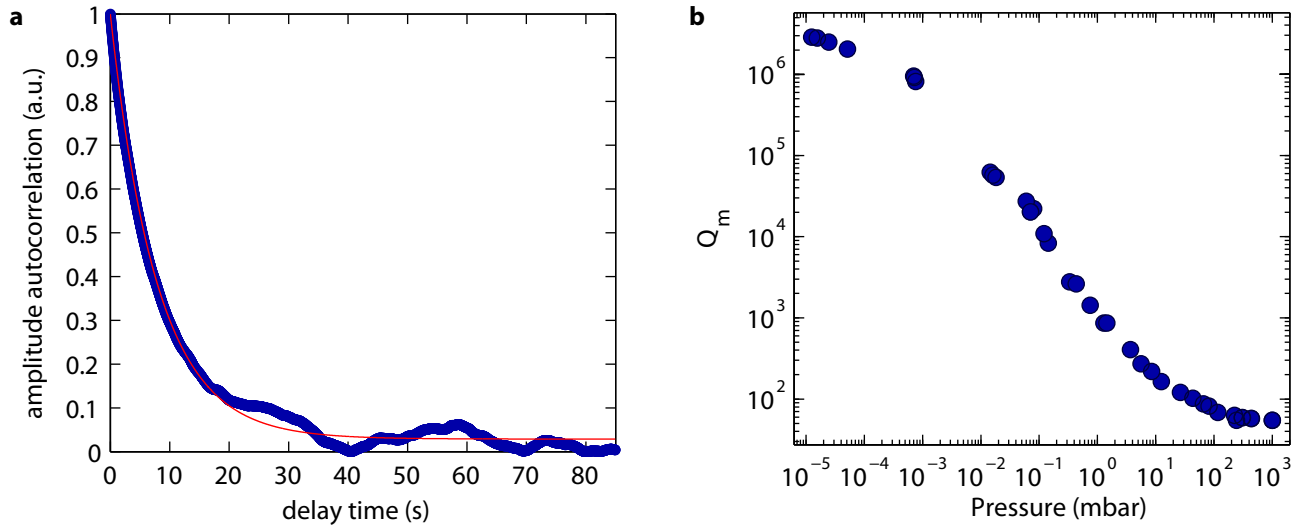

FIG. S2: **Investigation of mechanical Q-factors. a**, Autocorrelation trace of the thermal noise driven mechanical amplitude. The signal was obtained from computing the autocorrelation of the slowly varying magnitude of the mechanical motion returned from a lock-in amplifier, using the experimental set up of Fig. 2a in the main text. Fitting the trace with an exponential decay yields the time constant and thereby the mechanical Q-factor of the mode ($Q_m = 1.4 \times 10^6$). **b**, Pressure-dependence of the mechanical Q-factor of a control device with $m = 10^{-11}$ kg and 70 nano-tethers showing an increase from $Q \approx 53$ at ambient pressure to $Q \approx 2.5 \times 10^6$ in high vacuum.

DOI: 10.1038/NPHOTON.2012.245

IV. INVESTIGATION OF THE MECHANICAL Q-FACTOR

The sub-Hz linewidths of our mechanical modes make establishing the quality factor from a measurement of the power spectral density on a spectrum analyzer infeasible because it requires a fractional stability of the frequency to greater than $\gg 1/Q_m \approx 5\times10^{-7}$ over a period much longer than the decay time $Q_m/\omega_m > 10$ s. However, since the system is driven by a Gaussian thermal noise process, the autocorrelation of the amplitude $\langle X(t)X(t+\tau)\rangle$ can be shown to decay as $e^{-t/\tau}$ from which the quality factor can be obtained as $Q_m = \tau\omega_m$ (see Ref. [30] in the main text). The slowly-varying envelope of $\langle X(t)\rangle$ is obtained from the magnitude channel of a lock-in amplifier tuned to the mechanical resonance frequency with a bandwidth (≈ 100 Hz) much larger than the linewidth which ensures that small frequency diffusion does not affect the measurement of the envelope. To obtain the bare mechanical Q-factors the measurement is made at an optical power low enough to ensure there is no backaction. The autocorrelation is numerically computed and the decay is fit to an exponential curve with a constant (noise) offset. In Fig. S2a we show an autocorrelation trace of the device presented in the main text calculated from ≈ 3000 s of data sampled at 100 Hz and fit it to find $\tau = 7.85$ s and for $\omega_m = 2\pi\times 27.5$ kHz that $Q = 1.4\times10^6$. For lower-Q structures, it was confirmed that this technique agrees with a direct measurement of the linewidth from a spectrum analyzer.

Since gas damping severely limits the mechanical Q-factor of our oscillator, measurements were carried out in vacuum. Figure S2b shows pressure-dependent mechanical Q-factors using a device of equal mass as that presented in the main text but with 70 tethers, resulting in an eigenfrequency of $\omega_m = 2\pi\times 110$ kHz. We find that the device exhibits a Q-factor of 53 at ambient pressure which strongly increases when reducing the pressure in the vacuum chamber. In particular, for pressures below 10^{-3} mbar – the regime in which we carried out the measurements presented in the main text – we observe Q-factors above 10^6. These pressures are within range of modern packaging techniques for MEMS structures [2].

V. OPTOMECHANICAL AND THERMO-OPTICAL BACKACTION

The relatively small test mass makes the device studied in this work highly susceptible to optomechanical and thermo-optical back-action effects. Such dispersive couplings are well known to renormalize the frequency and damping rate of the mechanical oscillator. In particular, thermo-optical coupling which arises from a refractive index change of the material upon the absorption of cavity photons plays a significant role in these devices due to the efficient thermal isolation of our nano-tethered test-masses in vacuum. Previous studies have shown strong modification of the optomechanical spring effect and damping in similar zipper cavity devices (see Ref. [12] of the main text).

The Supplementary Information of Ref. [12] gives a detailed derivation of the renormalized oscillator frequency and damping rate under the influence of optomechanical and thermo-optical coupling. The system of differential equations that describes the time evolution of the intra-cavity field a, the oscillator position x, and the cavity temperature shift ΔT is given by

$$\dot{a} = -\left[i\Delta - (g_{\rm OM}x + g_{\rm th}\Delta T)\right]a - \frac{\kappa}{2}a + \sqrt{\frac{\kappa_e}{2}}a_{\rm in} \tag{S20}$$

$$\ddot{x} = -\gamma\dot{x} - \omega_m^2 x - \frac{\hbar g_{\rm OM}}{m}|a|^2 \tag{S21}$$

$$\dot{\Delta T} = -\gamma_{\rm th}\Delta T + \kappa_{\rm abs}c_{\rm th}\hbar\omega_c|a|^2, \tag{S22}$$

where $g_{\rm th} = -(dn/dT)(\omega_c/n)$ is the thermo-optical tuning coefficient, dn/dT is the thermo-optic coefficient of the material, $\kappa_{\rm abs}$ is the optical loss rate due to material absorption, $c_{\rm th}$ is the thermal heat capacity, and $\gamma_{\rm th}$ is the decay rate of the temperature. Linearizing these equations yields the static solutions

$$a_0 = \sqrt{\frac{\kappa_e}{2}}\frac{1}{i\Delta' + \kappa/2}, \quad x_0 = \frac{\hbar g_{\rm OM}}{m\omega_m^2}|a_0|^2, \quad \Delta T_0 = \frac{\kappa_{\rm abs}}{\gamma_{\rm th}}c_{\rm th}\hbar\omega_c|a_0|^2 \tag{S23}$$

with the renormalized detuning $\Delta' = \Delta - g_{\rm OM}x_0 - g_{\rm th}\Delta T_0$ arising from the static optomechanical and thermo-optical shift. Using a perturbation ansatz $x(t) = x_0 + \varepsilon\cos(\omega_m t)$ one arrives after some algebraic manipulation at a modified harmonic oscillator equation for x with a renormalized frequency ω_m' and damping rate γ' given by

$$\omega_m'^2 = \omega_m^2 - \frac{\hbar\omega_c n_{\rm cav}g_{\rm OM}^2}{\omega_c m}\,{\rm Im}\left[g(\omega_m)\right], \tag{S24}$$

$$\gamma' = \gamma + \frac{\hbar\omega_c n_{\rm cav}g_{\rm OM}^2}{\omega_m\omega_c m}\,{\rm Re}\left[g(\omega_m)\right], \tag{S25}$$

where the transfer function $g(\omega)$ is defined as

$$g(\omega) = f\frac{1 + f'^* f^*}{|1 + f' f|^2} \tag{S26}$$

with

$$f(\omega) = \frac{1}{i(\omega+\Delta')+\kappa/2} - \frac{1}{i(\omega-\Delta')+\kappa/2} \tag{S27}$$

and

$$f'(\omega) = -i\frac{\Delta_{\rm th}\gamma_{\rm th}}{i\omega+\gamma_{\rm th}}, \tag{S28}$$

and $\Delta_{\rm th} = g_{\rm th}\Delta T_0$ is the static thermo-optical shift of the cavity resonance frequency. In the sideband unresolved regime where $\omega_m \ll \kappa$ and for thermal decay rates $\gamma_{\rm th}$ smaller than the mechanical frequency, an approximation of $g(\omega)$ yields

$$\omega'^2 = \omega^2 + \frac{2\hbar n_{\rm cav} g_{\rm OM}^2}{m}\frac{\Delta'}{\Delta'^2+\kappa^2/4}\left[\frac{1+W}{1+s}\right], \tag{S29}$$

$$\gamma' = \gamma + \frac{2\hbar n_{\rm cav} g_{\rm OM}^2}{m}\frac{\kappa\Delta'}{(\Delta'^2+\kappa^2/4)^2}\left[\frac{1+V}{1+s}\right], \tag{S30}$$

with the correction factors

$$W = -\left(\frac{2\Delta_{\rm th}}{\kappa}\right)\left(\frac{\gamma_{\rm th}}{\omega_m}\right)^2\left(\frac{\kappa\Delta'}{\Delta'^2+\kappa^2/4}\right), \tag{S31}$$

$$V = \left(\frac{2\Delta_{\rm th}}{\kappa}\right)\left(\frac{\gamma_{\rm th}}{\omega_m}\right)^2\left(\frac{\Delta'}{\gamma_{\rm th}}\right) \tag{S32}$$

$$\tag{S33}$$

and the saturation parameter

$$s = \left(\frac{2\gamma_{\rm th}\Delta_{\rm th}\hbar\omega_c n_{\rm cav}}{\omega_m}\frac{\Delta'}{\Delta'^2+\kappa^2/4}\right)^2\left(1+\frac{1}{\Delta_{\rm th}}\left(\frac{\Delta'^2+\kappa^2/4}{\Delta'^2} - \frac{\omega_m^2\kappa}{\Delta'\gamma_{\rm th}}\right)\right) \tag{S34}$$

In the parameter regime of our devices, purely optomechanical back-action is a relatively weak effect due to the low optical Q-factor. For the parameters given above and for a pump laser with an incident power of $P_{\rm in} = 116\,\mu$W half a linewidth red-detuned from the cavity resonance, optomechanical back-action alone predicts a frequency shift of merely $\omega'_m - \omega_m = -2\pi \times 35.9$ Hz and a damping factor of $\gamma'_m/\gamma = 1.01$.

In order to study the influence of thermo-optical back-action, we measured the Q-factor of the mechanical mode as function of the optical power launched into the cavity, shown as the green bullets in Fig. S3. When increasing the optical power to $P_{\rm in} \approx 300\,\mu$W, which corresponds to an intracavity photon number of $n_{\rm cav} \approx 1{,}100$, the Q-factor shows strong damping and is reduced by a factor of ≈ 200. Similarly, we measure the area of the mechanical resonance peak from the optically transduced thermal noise PSD for a series of optical powers, and plot the inferred effective mode temperature as blue bullets in Fig. S3. Clear in Fig. S3 is that the effective mode temperature is dropping with the measured mechanical Q-factor.

The observed mechanical damping is much larger than the value predicted by pure optomechanical back-action and can be explained when including thermo-optical tuning. The green line in Fig. S3 was obtained by calculating the modified Q-factor $Q'_m = \omega_m/\gamma'_m$ using eq. (S25) with $\Delta_{\rm th} = -0.05\kappa$ and $\gamma_{\rm th} = 2\pi \times 9.2$ kHz. The latter value is in good agreement with the one from Ref. [12] ($\gamma_{\rm th} = 2\pi \times 10$ kHz), which suggests that the time constant of thermo-optical tuning is dominated by heat-flow from the zipper cavity region to the reservoir formed by the test-mass (or the bulk in the case of Ref. [12], respectively).

The obtained values for $\Delta_{\rm th}$ and $\gamma_{\rm th}$ result in correction factors of $V = 12{,}400$, $W = -0.011$, and a saturation parameter of $s \approx 3 \times 10^{-36}$. Accordingly, we expect a significant thermo-optical correction to damping, as observed, but only a minor modification of the optomechanical spring: $\omega' - \omega = 2\pi \times 36.2$ Hz for the pump power used in the experiment. Indeed, we observed a frequency shift of 101 Hz, in reasonable agreement with the theoretical value.

VI. ANALYSIS OF OPTICAL NOISE POWER SPECTRAL DENSITIES

As discussed in the main text, noise power-spectral-densities (PSDs), such as those shown in Fig. 2b, arise from the contributions of various noise sources. In the following we derive expressions for their magnitudes. Throuhgout the analysis below we work with single-sided PSDs, unless otherwise stated, as these are the PSDs measured in our experiment.

DOI: 10.1038/NPHOTON.2012.245

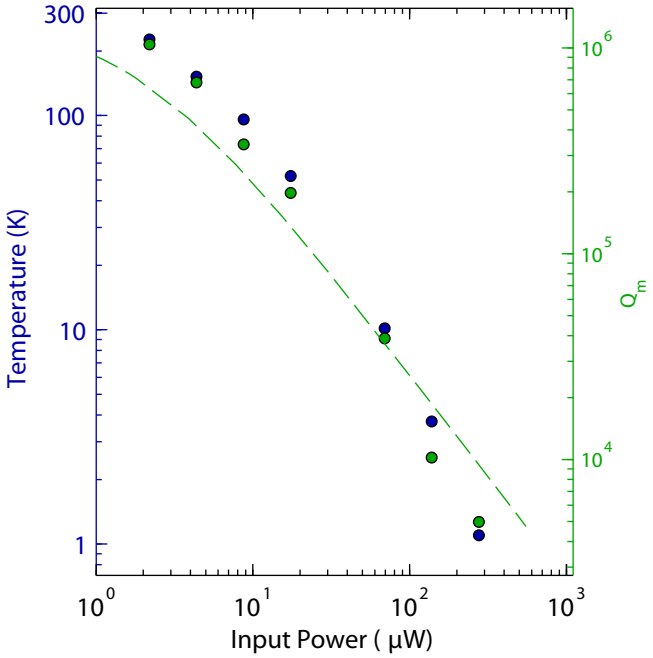

FIG. S3: **Demonstration of thermo-optomechanical damping and cooling.** The green bullets show measured Q-factors of the mechanical mode as function of the optical power, yielding thermo-optomechanical damping by a factor of ≈ 280. The blue bullets show the corresponding optical power in the sideband generated by mechanical motion, proportional to the effective mode temperature. We observe cooling to $T_{\rm eff} \approx 1$ K. The dashed green curve corresponds to a theoretical model that includes optomechanical and thermo-optical back-action.

A. Noise from thermal Brownian motion

In contact with a heat-bath at room temperature, the test-mass oscillator is subjected to thermal Brownian motion. From the equipartition theorem, the root-mean-square displacement of a harmonic oscillator is given by

$$x_{\rm rms} = \sqrt{\frac{k_{\rm B}T}{k}}. \tag{S35}$$

If we assume the acceleration-noise exerted by the bath to be white, i.e. frequency-independent, its power-spectral density S_{aa}^{th} has to obey

$$x_{\rm rms}^2 = \int_0^\infty |\chi(\omega)|^2 S_{aa}^{th}, \tag{S36}$$

such that thermal test-mass motion corresponds to a noise-equivalent acceleration (NEA) of

$$a_{\rm th} = \sqrt{S_{aa}^{th}} = \sqrt{\frac{4k_BT\omega_m}{mQ_m}} = \sqrt{\frac{4k_BT\gamma_m}{m}}. \tag{S37}$$

In the device presented in this work, we have $\omega_m = 2\pi \times 27.5$ kHz, $m = 10^{-11}$ kg, $Q_m = 1.4 \times 10^6$, $T = 295$ K, and therefore $a_{\rm th} = 1.4\ \mu{\rm g}/\sqrt{\rm Hz}$. For a mass-on-a-spring oscillator with $\omega_m = \sqrt{k/m}$ this corresponds to

$$a_{\rm th} = \sqrt{\frac{4k_BT}{Q_m}}\frac{k^{1/4}}{m^{3/4}}. \tag{S38}$$

Driving the harmonic oscillator with susceptibility $\chi(\omega)$, this NEA translates into frequency-dependent displacement noise according to

$$S_{xx}^{th}(\omega) = \frac{4k_BT\omega_m}{mQ_m}\frac{1}{(\omega^2-\omega_m^2)^2 + \left(\frac{\omega\omega_m}{Q_m}\right)^2}. \tag{S39}$$

According to eq. (S17), the optical signal transduced by the cavity then exhibits a noise power-spectral density of

$$S_{PP}^{th}(\omega) = \left|\frac{\mathrm{d}T}{\mathrm{d}\Delta}\right|^2 \eta_{\mathrm{in}}^2 P_{\mathrm{in}}^2 g_{\mathrm{OM}}^2 S_{xx}^{th} \tag{S40}$$

$$= (1-T_d)^2 \frac{Q^2}{\omega_o^2} \eta_{\mathrm{in}}^2 P_{\mathrm{in}}^2 g_{\mathrm{OM}}^2 \frac{4k_B T \omega_m}{m Q_m} \frac{1}{(\omega^2-\omega_m^2)^2 + \left(\frac{\omega\omega_m}{Q_m}\right)^2}. \tag{S41}$$

Under the influence of thermo-optomechanical back-action discussed above, the dynamic parameters ω_m and Q_m have to be replaced by the renormalized values ω_m' and Q_m'. With the parameter values realized in this experiment, the optical noise arising from thermal Brownian motion corresponds to $\sqrt{S_{PP}^{th}(0)} = 0.96\ \mathrm{pW}/\sqrt{\mathrm{Hz}}$.

B. Optical shot noise

Photon shot noise arises from the quantum nature of light and from the destructive character of optical measurements using photodiodes. The single-sided shot-noise power-spectral-density for light of frequency ω_o and power P_{det} incident on a photodetector is frequency-independent and given by

$$S_{PP}^{SN} = \frac{2\hbar\omega_o P_{\mathrm{det}}}{\eta_{\mathrm{qe}}}, \tag{S42}$$

where the quantum efficiency η_{qe} (=0.76) is linked to the photodiode responsivity R (=1 A/W) via

$$R = \frac{e\eta_{\mathrm{qe}}}{\hbar\omega_o}. \tag{S43}$$

In our balanced detection scheme, we consider the shot noise of the difference photocurrent of the two detectors. Since photon annihilation at the two detectors is uncorrelated, the total shot noise is given by the incoherent sum of the two individual power-spectral-densities, such that

$$S_{PP}^{SN} = \frac{2\hbar\omega_o P_{\mathrm{tot}}}{\eta_{\mathrm{qe}}} \tag{S44}$$

with $P_{\mathrm{tot}} = P_{\mathrm{det1}} + P_{\mathrm{det2}}$ being the sum of the individual powers hitting the two photodiodes. In our balanced detection scheme, $P_{\mathrm{det1}} = P_{\mathrm{det2}}$ and $P_{\mathrm{tot}} = 2T\eta_{\mathrm{in}}P_{\mathrm{in}}$. While the balanced detection scheme used in our experiment is beneficial towards the suppression of technical laser amplitude noise, it hence comes with the disadvantage of introducing more shot noise into the system. In this experiment, the noise-equivalent power corresponding to shot noise is 6.1 $\mathrm{pW}/\sqrt{\mathrm{Hz}}$. The noise-equivalent acceleration corresponding to this noise background is given by

$$a_{\mathrm{SN}}(\omega) = \sqrt{S_{aa}^{SN}} = \frac{1}{\left|\frac{\mathrm{d}T}{\mathrm{d}\Delta}\right| \eta_{\mathrm{in}} P_{\mathrm{in}} g_{\mathrm{OM}}} \frac{1}{|\chi(\omega)|} \sqrt{S_{PP}^{SN}} \tag{S45}$$

$$= \frac{\omega_o}{(1-T_d) Q_o g_{\mathrm{OM}}} \frac{1}{|\chi(\omega)|} \sqrt{\frac{2\hbar\omega_o(1+T_d)}{\eta_{\mathrm{qe}}\eta_{\mathrm{in}}P_{\mathrm{in}}}}. \tag{S46}$$

With the values given above, this yields $a_{\mathrm{SN}} = 8.9\ \mu\mathrm{g}/\sqrt{\mathrm{Hz}}$ around DC and $\sqrt{S_{xx}^{SN}(\omega_m)} = 3.1\ \mathrm{fm}/\sqrt{\mathrm{Hz}}$

C. Detector noise

The electronic detector noise is usually quantified by the noise-equivalent-power (NEP), which for the Newport 2117 detector and the transimpedance gain setting we use is on the order of 2.8 $\mathrm{pW}/\sqrt{\mathrm{Hz}}$. The optical noise power-spectral-density then is

$$S_{PP}^{NEP}(\omega) = \mathrm{NEP}^2. \tag{S47}$$

In analogy to eq. (S46), the NEA corresponding to electronic detector noise can be derived as

$$a_{\mathrm{NEP}} = \frac{\omega_o}{(1-T_d) Q_o g_{\mathrm{OM}} \eta_{\mathrm{in}} P_{\mathrm{in}}} \frac{1}{|\chi(\omega)|} \mathrm{NEP}. \tag{S48}$$

Here, this is found to be $a_{\mathrm{NEP}} = 4.1\ \mu\mathrm{g}/\sqrt{\mathrm{Hz}}$.

DOI: 10.1038/NPHOTON.2012.245

D. Backaction noise

The extra noise a_{add} added by the optical field mentioned in the main text arises from optical noise that exerts a random force on the mechanical oscillator via radiation pressure. The optical noise arises from classical amplitude noise and from intrinsic shot noise. In the following, we consider only quantum back-action noise a_{BA} arising optical shot noise. With $\hbar g_{\mathrm{OM}}$ being the force exerted per photon and for n_{cav} photons in the cavity, the random acceleration created by optomechanical back-action has a power spectral density of [1]

$$S_{aa}^{BA} = 2\frac{(\hbar g_{\mathrm{OM}})^2}{m^2} n_{\mathrm{cav}} \frac{4}{\kappa}, \tag{S49}$$

resulting in a noise-equivalent acceleration of $a_{\mathrm{BA}} = \sqrt{S_{aa}^{BA}} = 5.6\ \mathrm{ng}/\sqrt{\mathrm{Hz}}$. Here, owing to the low quality factor of the optical cavity and the low mechanical frequency, the shot noise radiation pressure force is approximately white noise for frequencies of relevance near the mechanical frequency. Note also that we are using single-sided PSDs, hence double the value of the (approximately) symmetric double-sided PSD. This value is much smaller than the acceleration noise created by the other sources discussed previously. The frequency-dependent displacement noise created by quantum back-action is

$$S_{xx}^{BA}(\omega) = 2\left(\frac{2\hbar g_{\mathrm{OM}}}{m}\right)^2 \frac{n_{\mathrm{cav}}}{\kappa} |\chi(\omega)|^2 \tag{S50}$$

On the mechanical resonance, and using eq. (S13), this yields

$$S_{xx}^{BA}(\omega_m) = 2\left(\frac{2\hbar g_{\mathrm{OM}} Q_m}{m\omega_m^2}\right)^2 \frac{1-\sqrt{T_d}}{\kappa^2} \frac{P_{\mathrm{in}}}{\hbar\omega_c}, \tag{S51}$$

resulting in $\sqrt{S_{xx}^{BA}(\omega_m)} = 23\ \mathrm{fm}/\sqrt{\mathrm{Hz}}$ for the device and experimental conditions described in Figs. 2 and 3 of the main text ($P_{\mathrm{in}} = 116\ \mu\mathrm{W}$). This should be compared to the fundamental standard quantum limited displacement noise given by

$$S_{xx}^{SQL}(\omega) = S_{aa}^{SQL} |\chi(\omega)|^2 \tag{S52}$$

$$= \frac{2\hbar\omega_m\gamma_m}{m} |\chi(\omega)|^2, \tag{S53}$$

which on resonance has the simple form

$$S_{xx}^{SQL}(\omega_m) = x_{\mathrm{zpm}}^2 \frac{4}{\gamma_m}, \tag{S54}$$

with the zero-point motion given by

$$x_{\mathrm{zpm}} = \sqrt{\frac{\hbar}{2m\omega_m}}. \tag{S55}$$

For the device and experimental conditions described in Figs. 2 and 3 of the main text, this yields an on-resonance SQL of $\sqrt{S_{xx}^{SQL}} = 2.8\ \mathrm{fm}/\sqrt{\mathrm{Hz}}$.

Note that although our back-action noise is above the SQL our shot-noise imprecision is not below the SQL due to optical losses. Only if single-sided coupling is employed and no photons are lost in the optical path can detection at the standard quantum limit be achieved. Here, optical losses arise both from taper losses and the inherent two-sided nature of our coupling scheme via the fiber taper.

E. General discussion

The dashed lines in Fig. 2b of the main text show the contributions of these noise terms to the PSD of the balanced photodetector output, where we neglected back-action noise. Figure S4a shows the corresponding frequency-dependent noise-equivalent acceleration values corresponding to the different noise terms for the device studied in the main text. Here, we include a_{BA}, which can be seen to only contribute negligibly to the NEA of the device. While a_{th} (green) and a_{BA} (gold) are frequency-independent, the NEAs of photon shot noise a_{SN} (red) and electronic detector noise a_{NEP} (cyan) are colored by the frequency-dependent response of the oscillator $\chi(\omega)$.

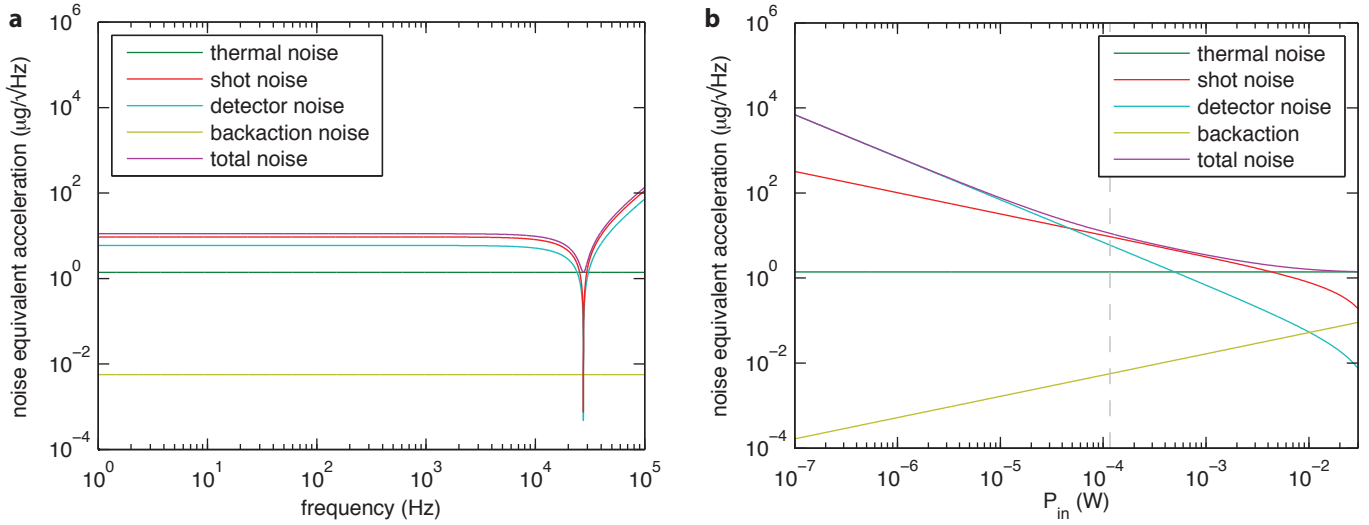

FIG. S4: **Frequency response of acceleration noise and power-scaling. a**, Frequency dependent contributions of different noise sources to the noise-equivalent-acceleration (NEA). For this calculation, we used the same parameters as for the device shown in Fig. 2 of the main text. **b**, Dependence of the DC-NEAs as function of incident laser power. The dashed vertical line indicates the optical power used in measurements of Figs. 2 and 3 of the main text.

While thermal noise arises as a fundamental property of a mechanical oscillator in contact with a heat bath at temperature T, the contributions of shot noise and detector noise are dependent on the efficiency of the optomechanical transduction mechanism. From eq. (S46) and eq. (S44), one can see that $a_{\rm SN} \propto P_{\rm in}^{-1/2}$, while from eq. (S48) it follows that $a_{\rm NEP} \propto P_{\rm in}^{-1}$. Similarly, back action noise scales with the square-root of the number of photons in the cavity: $a_{\rm BA} \propto P_{\rm in}^{1/2}$. For illustration, Fig. S4b shows the relative contributions of the individual noise terms at DC ($\omega = 0$) as function of incident power. Here, we include the effects of thermo-optomechanical back-action on the mechanical susceptibility, as discussed in sec. V. The thermal noise background is not affected by cooling of the mechanical mode, since it follows from eq. (S37) that $a_{\rm th}^2 \propto T_{\rm eff}\gamma_m = {\rm const}$ under back-action damping/cooling of the mechanical mode. The roll-off of shot noise and detector noise for pump powers above 10 mW arises from the decrease of the mechanical mode frequency ω_m' due to the optomechanical spring effect. This results in an increase of the DC acceleration sensitivity $\chi(0) = 1/{\omega_m'}^2$ and thereby a reduction of the corresponding acceleration noise floors according to eqs. (S46) and (S48).

As mentioned previously, for the power used in the experiment, the NEA is limited by photon shot noise. For two orders of magnitude higher pump powers, the NEA starts being dominated by thermal noise of the test-mass oscillator. Alternatively, according to eq. (S46), thermal-noise limited detection can be achieved by increasing $g_{\rm OM}$ by one order of magnitude.

F. Analysis of noise sources present in the experiment

As shown in Fig. S4, shot noise is theoretically the dominant noise source away from the mechanical resonance. Indeed, we find that this is the case in our experiment for a large range of frequencies. In separate measurements, we recorded the optical noise power spectral density over a range of optical powers for three different gain settings of our balanced photodetector, as shown in Fig. S5. At each gain setting, the optical noise power spectral density (blue data points) rises from an offset due to detector noise, which allows us to determine the detector NEP (dashed cyan line). At larger powers, the optical noise spectral density scales as the square root of the input power, as expected for shot noise. The red dashed line shows the theoretical calculation of shot noise from eq. (S44). Fitting the power dependence of the noise floor (dashed black line) therefore allows us to calibrate both the NEP for each gain setting and the responsivity (and thereby the quantum efficiency η) of our detector. The calibrated values for the NEP and the responsivity were used for the theory-curves in Fig. 2b, Figs. 3a,3b, and Figs. S4a.,S4.b, where we used a detector gain setting of $g = 100$.

In addition to the flat background given by shot noise, we find a series of extra noise features in the optical PSD shown in Fig. 2b of the main text. These are primarily manifested in a series of sharp resonances as well as an increase of the noise background for frequencies below ≈ 3 kHz. In order to identify the source of these extra noise features as arising from the fibre taper, we independently measured the response of the fibre taper transmission to accelerations applied via the shake table. This is achieved by measuring a noise spectrum like in Fig. 3a of the main text, yet with the laser approximately 2 nm detuned

DOI: 10.1038/NPHOTON.2012.245

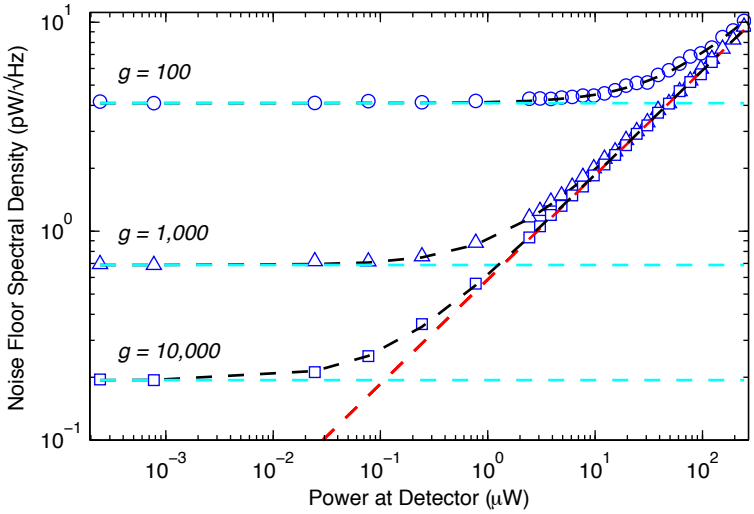

FIG. S5: **Measured optical power spectral density noise floor versus optical power.** Blue circles (triangles, squares) show noise measurements for detector gain settings of 100 (1000, 10,000) respectively, with the gain setting of 100 being used in the experiments described in the main text. The cyan dashed lines show the extracted NEP (noise equivalent power) values of the detector at each gain setting. The red line is a calculation of the expected shot noise, showing scaling with $\sqrt{P_{\mathrm{det}}}$, whose fit allowed the extraction of the detector's quantum efficiency. The black lines show the incoherent sum of shot noise and detector noise and agrees very well with the data.

from the cavity resonance to eliminate any pick-up from the zipper cavity. The green curve in Fig. S6 shows data obtained in this manner. Clearly, the bare fibre taper exhibits a substantial response to applied accelerations, which we attribute to optical losses into the substrate that are modulated by the mechanical motion of the taper. This response contains both a series of sharp resonances and a low-frequency feature that follows an ω^{-2} dependence like the response of a low-lying mechanical resonance. The response (i.e. the sensitivity) of the accelerometer taken with the laser on resonance – shown in Fig. 3a of the main text and repeated in Fig. S6 as the blue line for comparison – follows the frequency-dependence of the fibre taper for low frequencies,

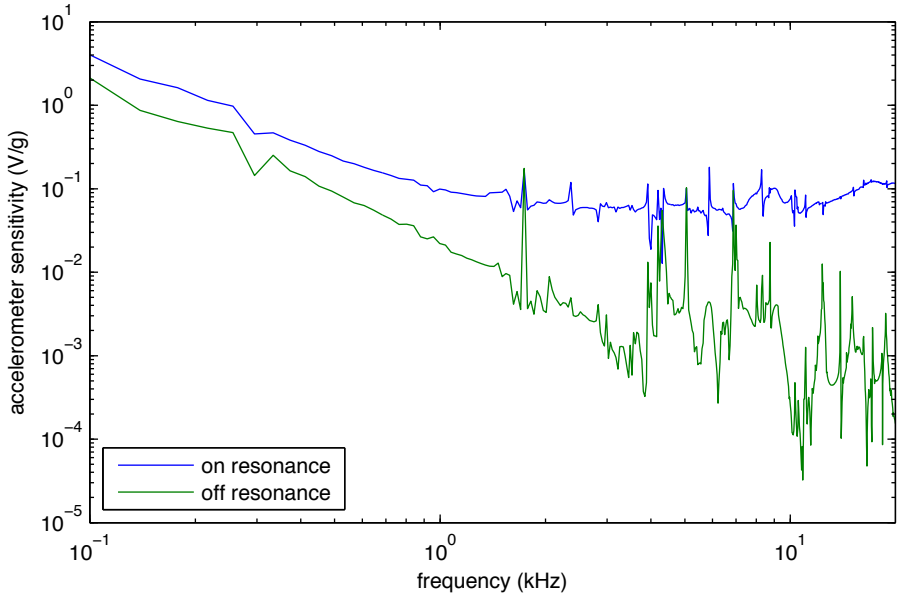

FIG. S6: **Comparison of the low-frequency on and off resonance response of the accelerometer and the bare fibre taper.** The blue curve is the low-frequency zoom-in of the data shown in Fig. 3a of the main text and is taken with the laser half a linewidth red-detuned from the cavity resonance. The green curve was obtained by detuning the laser far from the optical resonance and thus excludes any transduction from the optomechanical accelerometer. This curve shows a pronounced ω^{-2} dependence, thus suggesting that the response is dominated by a low-frequency mechanical mode of the taper.

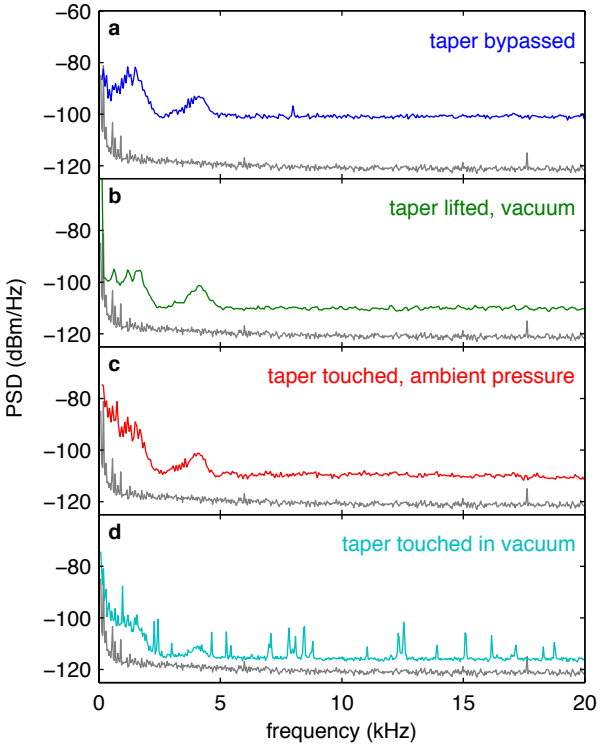

FIG. S7: **Optical noise PSDs for different experimental configurations.** The blue curve is the noise PSD present in the detection system with the taper bypassed. The green curve shows the response with the taper in-line but far from the sample surface. The red curve shows the response with the taper touched down to the sample in ambient pressure, exhibiting an increased DC noise level. The cyan curve shows the response with the taper touched down in vacuum and the laser detuned from the optical resonance. Taken together, these curves suggest that the sharp resonances are due to mechanical modes of the taper whose Q-factors are enhanced in vacuum, and, the low frequency noise ($\lesssim$ 1 kHz) (while present without the taper) is enhanced by the proximity of the taper to the substrate.

yet exhibits a sensitivity increased by roughly a factor of two with respect to the bare taper response. We attribute this increase by an optomechanical coupling between motion of the fibre taper and the optical cavity resonance.

In order to gain further insight into the influence of the fibre taper on the noise performance of our device, we compare noise power spectral densities for different arrangements of the fibre taper waveguide with respect to the zipper cavity, as shown in Fig. S7. The blue curve in Fig. S7a shows the inherent noise background of our measurement system, obtained by recording the balanced photodiode signal when bypassing the fibre taper. The gray curve for comparison shows the electronic noise background of the detector in the absence of optical signals. The detector exhibits characteristic $1/f$-noise and creating a noise background well below the optical signal. From the blue curve it can be seen that while for frequencies above $\sim$ 5 kHz the signal is dominated by photon shot noise, there are two prominent noise features at 1 kHz and 4 kHz that arise from acoustic noise in the laboratory transduced by elements in the optical train such as the fibre beamsplitter and the laser head. This identification was established by employing a tunable frequency sound generator while observing the magnitude of the corresponding modulation tone in the optical PSD. We found substantial enhancement of this acoustic pick-up when the sound frequency was resonant with the features in Fig. S7, and in particular when the speaker was placed close to the fibre beamsplitter and laser head.

The green curve in Fig. S7b shows a PSD with the taper in the optical path, yet hovering several 100 μm above the sample. In this situation, we observe a qualitatively similar spectrum to the one before, yet with a slightly enhanced response at low frequencies. We note that the power at the detector was different in these four experiments, explaining the difference in background noise levels. The red curve in Fig. S7c shows a PSD with the taper touched down near our device at ambient pressure with the laser off-resonance from the cavity mode. Here, we notice a strong increase of noise below $\sim$ 1.5 kHz. We interpret this increase as an enhancement due to the $1/\omega^2$ response of the taper discussed above that arises when the taper is evanescently coupled to the substrate. Finally, the cyan curve in Fig. S7d shows a noise spectrum obtained under the same conditions as our experiment, i.e. with the taper touched down near the device in vacuum, yet the laser detuned from the cavity resonance. Here, we observe the emergence of a series of sharp resonances, leading us to conclude that the same features observed in the experiment are of mechanical origin, and their appearance in vacuum is caused by an increase of their quality factors.

Test measurements with commercial accelerometers – as shown in the inset of Fig. 3a of the main text – confirm that these sharp resonances do not arise from the shake table. Also, the extra noise in vacuum does not arise from the vacuum pump,

DOI: 10.1038/NPHOTON.2012.245

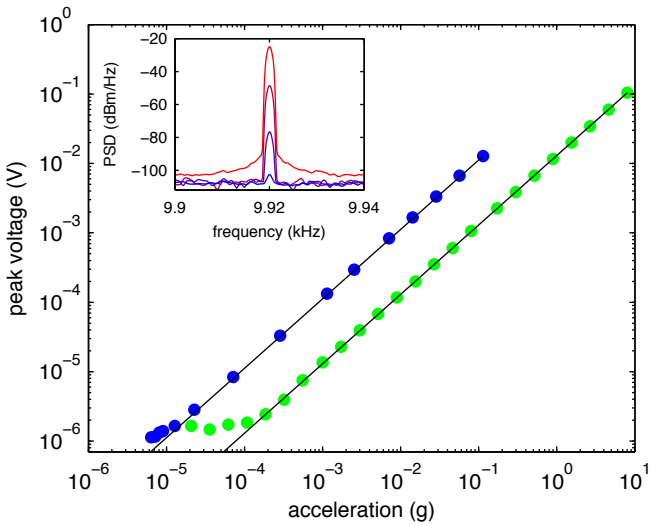

FIG. S8: **Demonstration of large linear dynamic range of typical devices.** While varying the amplitude of the acceleration applied with the calibrated shake table at 9.92 kHz, we measure the optical signal transduced via the mechanical mode. The blue bullets show the transduced signal of the device presented in the text using the voltage corresponding to the peak height of the modulation tone on the ESA spectrum, which exhibits linear response over 40 dB. The inset shows the corresponding PSD spectra from the ESA for modulation tones between 0.1 g and 12.8 μg, taken at a resolution bandwidth of 1 Hz. The green bullets show data obtained from a different device (with relevant parameters $g_{\rm OM}/2\pi = 6.36$ GHz/nm, $\omega_m/2\pi = 27.5$ kHz, $\lambda_o = 1539$ nm, $Q_o = 3000$, and $Q_m = 13{,}000$) with a larger thermal noise background but very similar optomechanical coupling using the lock-in scheme depicted in Fig. 2 of the main text, which exhibits linear response over 49 dB – limited by the maximum voltage output of our function generator, which corresponds to an acceleration of 8 g. The black lines are linear fits to the data.

because we use an ion getter pump with no moving parts. Moreover, we found that different ways of touching the fibre taper on the device results in shifts both in amplitude and frequency of these extra noise modes. In combination, these observations strongly support the existence of extra noise channels introduced by mechanical modes of the fibre taper.

VII. LINEAR DYNAMIC RANGE

A key requirement for any inertial sensor is linear response over a reasonable dynamic range. To check the linearity of the response of the accelerometer presented in the text, we varied the amplitude of a sinusoidal signal sent to the shear piezo at 9.92 kHz and recorded the voltage corresponding to the peak height of the transduced modulation tone – shown in blue bullets in Fig. S8. The sensor behaves linearly over a dynamic range of 41 dB, with the tone vanishing into the shot noise floor for an applied acceleration of ≈ 10 μg at a resolution bandwidth of 1 Hz. The green bullets in Fig. S8 show data from a different device with similar geometry but lower mechanical Q-factor (with relevant parameters $g_{\rm OM}/2\pi = 6.36$ GHz/nm, $\omega_m/2\pi = 27.5$ kHz, $\lambda_o = 1539$ nm, $Q_o = 3000$, and $Q_m = 13{,}000$), which exhibits a linear response over 49 dB. This particular measurement was limited by the maximum output voltage of the function generator. Ultimately, however, the linear dynamic range ends when motion of the test mass shifts the optical resonance by a magnitude comparable to the optical cavity linewidth. For drive frequencies substantially below the resonance frequency, an acceleration of ~ 30 g moves the cavity resonance over one linewidth, κ.

[1] Clerk, A. A., Devoret, M. H., Girvin, S. M., Marquardt, F., & Schoelkopf, R. J. Introduction to quantum noise, measurement, and amplification. *Rev. Mod. Phys.* **82**, 1155–1208 (2010).

[2] Sparks, D., Massoud-Ansari, S., & Najafi, N. Chip-Level Vacuum Packaging of Micromachines Using NanoGetters. *IEEE Trans. Adv. Packag.* **26**, 277–282 (2003).